

# Characterization of Microstructure and Mechanical Properties of Friction Stir Welded Reduced Activation Ferritic–Martensitic Steel in As-Received, As-Welded and Post-weld Heat-Treated States

Johny Varghese<sup>1</sup> · Koteswararao V. Rajulapati<sup>1</sup> · K. Bhanu Sankara Rao<sup>1</sup> · N. Chavan Akash<sup>1</sup> · S. D. Meshram<sup>2</sup> · G. Madhusudhan Reddy<sup>2</sup>

Received: 10 April 2022 / Accepted: 29 April 2022 / Published online: 25 May 2022  
© The Indian Institute of Metals - IIM 2022

**Abstract** In this paper, an attempt has been made to explore the feasibility of employing friction stir welding (FSW) of 12-mm-thick reduced activation ferritic–martensitic (RAFM) steel plates using a polycrystalline cubic boron nitride (PCBN) tool at a rotation speed of 200 rpm. Deep penetration bead-on-plate welds were successfully produced. Microstructures evolved in stir zone (SZ), thermomechanically affected zone (TMAZ), heat-affected zone (HAZ) and unaltered base metal zones, and their impact on microhardness was assessed. The SZ and TMAZ revealed high hardness, while HAZ became much softer than the base metal. Several grain boundaries in SZ and TMAZ were found to be free from carbides, and SZ contained martensite laths, Fe<sub>3</sub>C needles and very high dislocation density. HAZ displayed coarse and coagulated carbides. The inhomogeneous microstructure and hardness variation across the weld joint have been rectified by appropriate post-weld normalising and tempering (PWNT) treatment. Tensile tests were conducted at room and elevated temperatures (450 °C, 500 °C, 550 °C) on transverse samples profiled from as-welded and PWNT states; and the displayed stress–strain behaviour and mechanical properties were compared with those obtained concurrently on base metal at various temperatures. The observed tensile hardening/softening as a function of temperature has been explained based on the substructure evolution. It has been noticed that the variation of the fraction of low-angle grain

boundaries and high-angle grain boundaries played a significant role in influencing the tensile deformation behaviour in the as-welded and PWNT states. The low ductility observed at 450 °C has been ascribed to dynamic strain ageing. Alloy displayed ductile fracture, in spite of variation in tensile properties depending upon the state of the material and tensile test temperature. This is the first ever investigation dealing with the tensile behaviour of friction stir welded RAFM steel under different states and conditions.

**Keywords** RAFM steel · 12 mm thick · Friction stir welding · Tensile properties · Microstructure · Dimple fracture

## 1 Introduction

The research for harvesting energy on a commercial basis from the fusion reactors is being pursued very intensively worldwide. International Thermonuclear Experimental Reactor (ITER) is currently under construction for conducting feasibility studies on the production of fusion energy and screening different concepts utilizing test blanket modules for tritium breeding in a fusion environment. The components of the first wall, divertor, limiters and blanket modules are subjected to high neutron irradiation, in addition to strong thermal, mechanical and electromagnetic loadings. The structural materials also should have the least activation from the consideration of nuclear waste disposal and decommissioning at the end of service. The main task in materials programme for TBMs is to comply with safety conditions by developing reduced activation materials. Several alloys have been suggested to be used in these situations out of which reduced activation

✉ Koteswararao V. Rajulapati  
kvrse@uohyd.ac.in

<sup>1</sup> School of Engineering Sciences and Technology, University of Hyderabad, Hyderabad 500046, India

<sup>2</sup> Defence Metallurgical Research Laboratory, Hyderabad 500050, India

ferritic/martensitic (RAFM) steels have been proved to be much propitious because of their proven ability to meet the required microstructure and mechanical properties at operating temperatures of ITER. Majority of the participating countries have developed their own compositions for RAFM steels [1–5]. India has pursued a systematic and comprehensive investigations and frozen the composition of its RAFM steel and designated it as IN-RAFM steel [6–9]. The composition of IN-RAFM steel was derived from the conventional modified 9Cr-1Mo steel by replacing the highly radiation-sensitive elements Mo, Nb by W and Ta, and exercising strict control over C, N, S, P and other trace and tramp elements [10]. Such control over chemistry was necessary for lowering induced radioactivity [10]. The careful choice of virgin materials with low impurities and melting by VIM and VAR enabled to achieve very low ductile-to-brittle transition temperature, and also parent improved the creep-rupture strength and ductility at elevated temperatures.

The RAFM steel which will be used to manufacture the first wall and blanket structure of a fusion reactor needs to be joined by an appropriate joining method during the manufacturing process. This joining method should not be harming the base metal properties for which the RAFM steel is tailor-made. The conventional fusion welding methods like TIG, MIG, EBW, etc., have been investigated, and there is considerable change in the microstructure and mechanical properties of the weld compared with the base metal. Moreover, as these welding techniques involve the melting of the parent metal, the presence of  $\delta$ -ferrite which is a deleterious phase was reported in most of the weldments. Therefore, there is a need for a welding method that can avoid these issues. Friction stir welding (FSW) holds a better promise in this regard. FSW is a solid-state welding process that does not involve the melting of the parent metal. Coalescence is produced by the frictional heat developed between the rotating welding tool and workpiece [11–13]. Obtaining a defect-free weld depends upon the proper choice of tool material, optimization of welding parameters like tool rotation speed, tool traverse speed, tool tilt angle, etc.

Studies were carried out [14–16] on the feasibility of FSW of RAFM steel and optimised the process parameters for 6-mm-thick plates. The welding of thicker plates (> 6 mm) using FSW is a challenging task as the tool rotation speeds required are high in order to create the local softening in thick plates for facilitating the material transport while stirring. Successful FSW joints between 12-mm-thick plates have been realized by employing tool rotation speeds of 500 and 900 rpm at a traverse speed of 20 mm min<sup>-1</sup>; at these high rotational speeds, the heat input was found high and led to higher width of the very soft and undesirable heat-affected zone (HAZ) [15, 17].

The tensile properties of such type of FSW welds have not been explored yet.

In order to avoid very wide and soft HAZ, an attempt has been made in this investigation for producing sound bead-on-plate welds on 12-mm-thick RAFM steel at a slow tool rotational speed of 200 rpm. The microstructures in the as-received (AR), as-welded (AW) and post-weld heat treatment (PWHT) conditions in various zones of FSW joint have been evaluated and correlated with the hardness. Changes that occurred in the grain size and substructure evolution in various zones have been studied in detail and reported. The tensile properties of AW and PWHT states at various temperatures on RAFM plates of 12 mm thickness are being reported for the first time.

## 2 Experimental Details

RAFM steel plates of 12 mm thickness were manufactured at MIDHANI, Hyderabad, India, and supplied in bulk to Institute of Plasma Research (IPR) Gandhinagar, India. In the current investigation, 300 × 300 mm square blanks of 12 mm thickness procured from IPR were utilised. The steel was supplied in normalized (980 °C/30 min + air cooling) and tempered (760 °C/90 min + air cooling) condition. The chemical composition of the alloy determined by optical emission spectroscopy technique is shown in Table 1.

FSW was carried out with the equipment supplied by Manufacturing Technology Inc., USA, in the position control mode (Fig. 1a). Bead-on-plate FSW experiments were performed employing polycrystalline cubic boron nitride tool; the geometry and dimensions of PCBN tool are given in Fig. 1b. All FSW beads were obtained by employing the tool rotating speed of 200 rpm, with a tool traverse speed of 15 mm min<sup>-1</sup> and tilt angle of 2°. The chosen tool traverse speed produced welds without defects and also ensured no damage to the tool. The FSW bead surface was protected during welding by providing argon gas shielding. Figure 2a depicts a macrograph revealing various zones (SZ, TMAZ, HAZ and BM) in the transverse cross section of FSW joint.

Etching was performed using Vilella's reagent (100 ml Ethanol, 5 ml HCl, 1 g picric acid) on mirror polished samples to observe the post-weld microstructure using optical and FESEM techniques. Electron micrographs were obtained using FEI-Nova nano-SEM 450 machine. The Vickers hardness of the weldment was studied using a machine manufactured by M/s. Tinius Olsen. Indents at regular intervals towards both sides from the centre of the weld were taken. TEM samples were prepared by polishing the weldment to a thickness of 100 microns using emery papers of different grit sizes. The thinned weldment was

**Table 1** Chemical composition of INRAFM steel used in this investigation

Element	Weight %	Element	Weight %
C	0.077	Ni	0.018
Mn	0.537	Mo	0.002
Si	0.021	Cu	0.001
S	0.002	V	0.246
P	0.004	W	1.360
Co	0.007	Cr	9.130
Ta	0.066	Fe	88.602

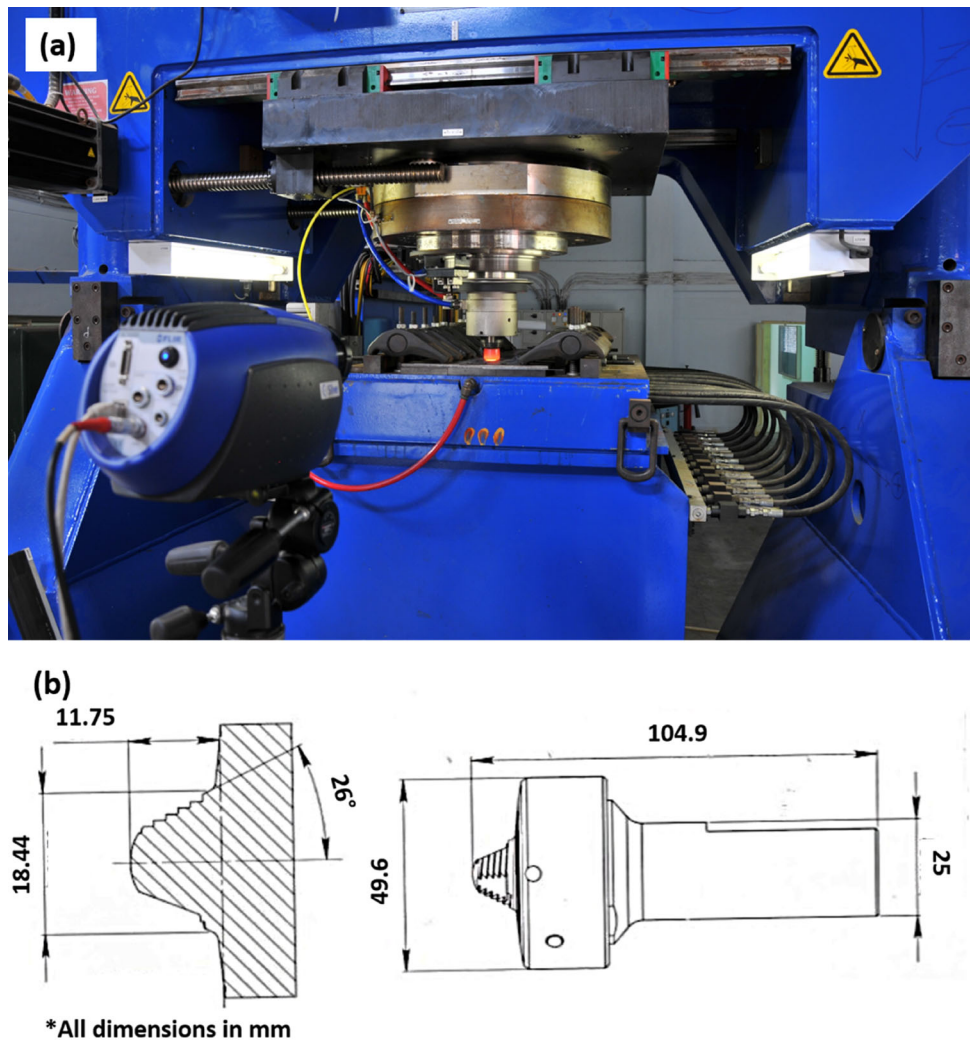
punched to discs of 3 mm diameter and was subjected to dimpling using a GATAN dimple grinder (model: 623). The dimpled discs were milled in a GATAN precision ion polishing system (PIPS). These discs were subjected to

transmission electron microscopy (TECHNAI FEI G2 S-Twin) at an accelerating voltage of 200 keV.

The welded plates were subjected to post-weld normalizing followed by tempering (PWNT) heat treatment, in which the plates are heated to the solutioning temperature of 980 °C and soaked for 30 min and then air-cooled. After this, a tempering treatment at 760 °C is given for 90 min, followed by air cooling. The optimum parameters for PWNT were established earlier for this alloy [14]. Nabertherm muffle furnace (model: LT 15/13) which has a temperature accuracy of ± 1 °C was used for the heat treatments.

Tensile specimens according to the ASTM E8-M standard were machined from the AR, AW and PWNT plates using EDM wire-cut method. The machined specimens were ground for better surface finish and dimensional homogeneity. Figure 2b shows the dimensions of the tensile specimen used in this study. The gauge portion of

**Fig. 1** a Friction stir welding setup, b geometry of polycrystalline cubic boron nitride tool





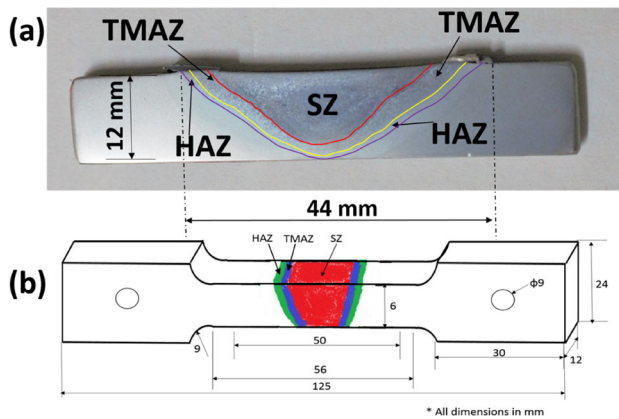


**Fig. 2** **a** Various zones in the friction stir welded bead-on-plate of 12 mm thickness, **b** geometry of tensile testing specimen

tensile samples was composed of SZ, TMAZ, HAZ and BM. Tensile testing was carried out employing Instron 5982 UTM with a maximum capacity of 100kN. Appropriate extensometers were used to accurately measure the elongation in the gauge length region. Tensile tests were carried out at room temperature and at 450, 500, 550 °C in AR, AW and PWNT states. The fractured samples were observed under SEM in order to obtain the information on the mechanism of failure.

EBSA analysis was done on the samples in the AW and PWNT states in the constituent zones. FE-SEM equipped with an EBSD detector manufactured by EDAX was used for this study. The samples were hot mounted using Bakelite powder, and vibratory polishing using colloidal silica of particle size 0.05 microns was given for 14 h in a vibratory polishing machine manufactured by QATM, Germany, before EBSD mapping. Fractions of high-angle grain boundaries and low-angle grain boundaries were deduced in the AR, AW, and PWNT conditions in different zones; the variation in these fractions between BM, AW and PWNT were analysed to explain the mechanical property variations.

### 3 Results and Discussion

#### (A) Initial Microstructure

The microstructure in AR state consisting of tempered lath martensite is revealed in Fig. 3. The discrete precipitates on grain boundaries have been identified as chromium-rich  $M_{23}C_6$  type carbides, while the intragranular regions display both  $M_{23}C_6$  type carbides and fine MC or carbonitrides rich in V or Ta (Fig. 3 a & b). In general, the lath boundaries in intragranular regions are found decorated with  $M_{23}C_6$ . The high creep resistance of tempered lath martensite structure has been attributed to its stability over

very long durations and results from combined influence of homogeneous distribution of the nanoscale precipitates within the tempered martensite matrix as MC type carbides and as discrete  $M_{23}C_6$  particles precipitating on the boundaries of prior austenitic grains and laths. Intra-lath regions have also contained individual dislocations and dislocation tangles. The grain boundary carbides provide the desired creep resistance by impeding the grain boundary sliding at operating temperature of the steel. In the AR state, the steel displays an average linear intercept grain size of approximately 7 microns. The width of the tempered martensite laths vary in the range of  $\sim 480 \pm 70$  nm.

#### (B) Microstructure in Different Zones After FSW

The macrostructure of the weld comprising of different zones is schematically described in Fig. 2a. The centre of the weldment where the tool pin rotates is SZ. The region next to the SZ is TMAZ. This region can be attributed to the area where the mechanical effects of the stirring action of the tool and the temperature effects due to the frictional heat developed by the rotating tool have jointly prevailed. The region next to the TMAZ is HAZ. In this region, there is no mechanical effect of the rotating tool, but the heat

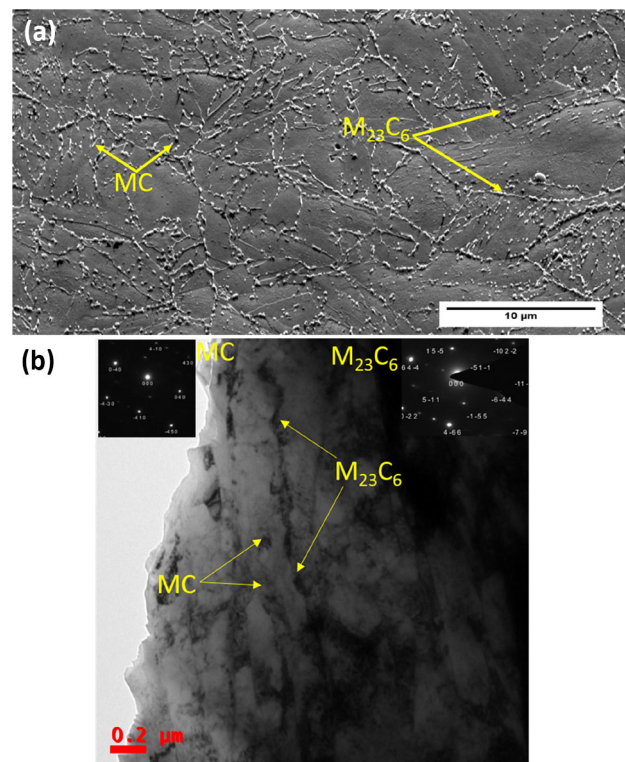


**Fig. 3** **a** As-received FE-SEM micrograph showing  $M_{23}C_6$  on prior austenitic grain boundaries and both MC and  $M_{23}C_6$  precipitates in intragranular regions, **b** TEM micrograph displaying both MC and  $M_{23}C_6$  on lath and intra-lath regions and large number of dislocations and dislocation tangles in intra-lath regions

experienced will promote microstructural changes in HAZ. The region that is far from the centre of the weld and is next to the HAZ is the unaffected BM. The welded blanks for tensile samples were machined in transverse direction; the orientation of tensile sample was perpendicular to the tool traverse direction.

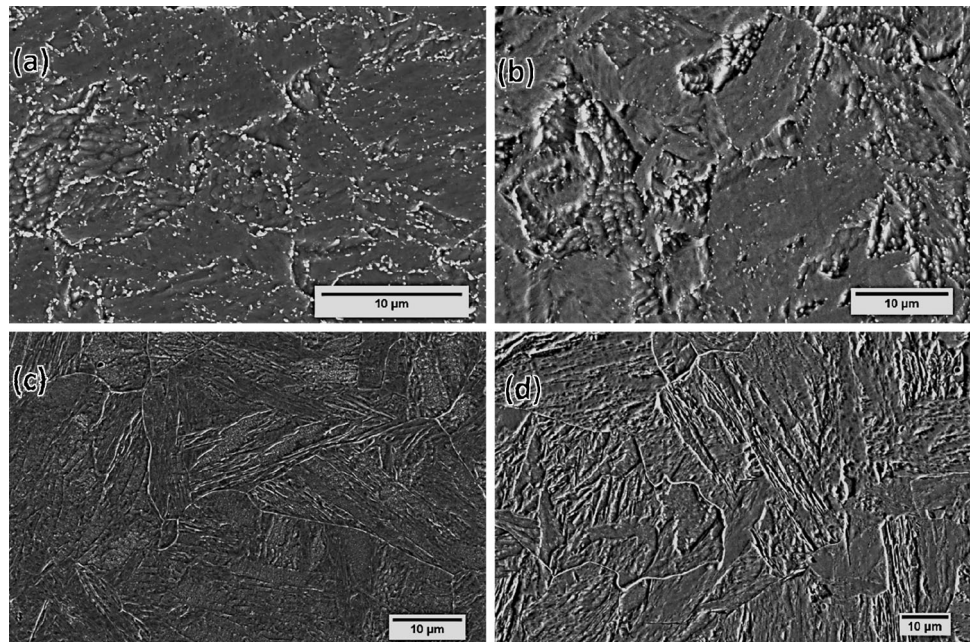
The FE-SEM microstructures in different zones of the weld are depicted in Fig. 4. The microstructure of the BM region resembles that of the initial material's (AR) microstructure. It is noticed that most of the grain boundary carbides which are present in the base metal (Fig. 4a) have disappeared in the TMAZ (Fig. 4c) and SZ (Fig. 4d). There has not been much change in the prior austenite grain size between BM and SZ; the inference from this observation is that, the temperature in stir zone has not attained to a level where it can cause rapid grain growth.

Evaluation of microstructure by TEM in SZ in the AW state indicates the presence of freshly formed martensite plates in the alpha-ferrite matrix, few undissolved MC particles, dislocation cell structure, high dislocation density in cell interiors and  $\text{Fe}_3\text{C}$  which is formed along  $\{0-31\}$  zone axis (Fig. 5). The occurrence of these features can be rationalised based on the interface temperature experienced between the top surface of the plate and bottom surface of the tool shoulder. In detailed investigations performed on this steel of 6 mm plate thickness, the interface temperature has been shown to depend upon heat input dictated by tool rotational speed [16]; the tool rotational speeds of 200, 300–500 and 700 rpm record interface temperatures below

$A_{c1}$  (lower critical temperature), between  $A_{c1}$  and  $A_{c3}$ , and above  $A_{c3}$  (upper critical temperature), respectively, with reference to Fe–C phase diagram. Various transformation temperatures for RAFM steel that have been determined earlier [9] are given in Table 2.

In general, phase transformation occurs by heating above the  $A_{c1}$  transformation temperature at which austenite begins to form on heating. Since the prior austenite grain size of SZ and BM are similar, it can be presumed that in the SZ of 12-mm-thick plate, the interface temperature has not exceeded above  $A_{c3}$ . The occurrence of fresh martensite (Fig. 5) suggests that the minimum temperature attained in SZ is above  $A_{c1}$ . This observation acts as a pointer to that in 12-mm-thick plate, the interface temperature is in intercritical zone bounded by  $A_{c1}$  and  $A_{c3}$ . This observation leads to a conclusion that the interface temperature can also be a function of the section thickness of the steel. The nucleation of austenite takes place at alpha grain boundaries in SZ, when the interface temperature is in the intercritical zone. Subsequently, on cooling, the freshly formed austenite undergoes phase transformation leading to the occurrence of martensite, as detailed in Fig. 5. It has been opined that the major driving force for  $\text{Fe}_3\text{C}$  precipitation in SZ is carbon supersaturation [14, 16]; an increase in the carbon concentration in the matrix would favour this type of carbide. Majority of the  $\text{M}_{23}\text{C}_6$  precipitates in the SZ during FSW deformation would be fragmented to a size which makes them to be subcritical. These subcritical particles undergo a solid-state

**Fig. 4** FE-SEM micrographs of AW 12 mm plate **a** base metal showing tempered martensite structure, **b** heat-affected zone showing coarsening and coalescence of  $\text{M}_{23}\text{C}_6$ , **c** thermo-mechanically affected zone, and **d** stir zone. SZ and TMAZ show precipitate-free grain boundaries





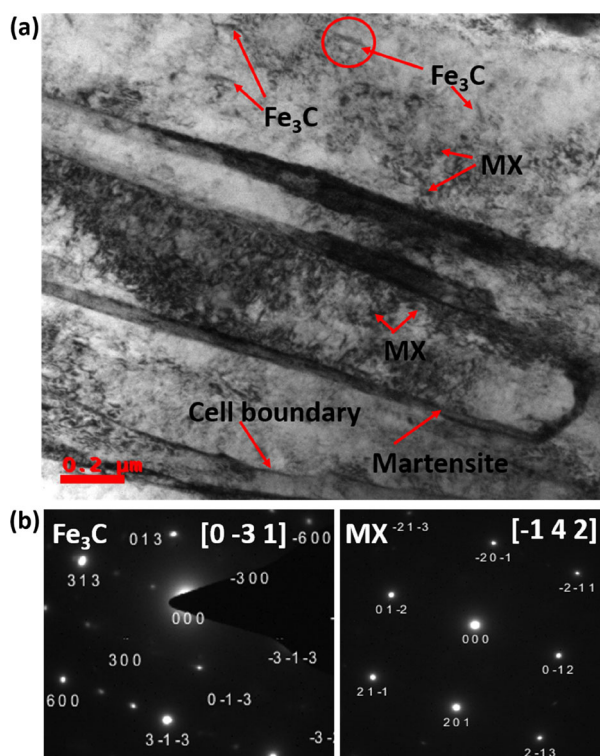


**Fig. 5** TEM micrograph of SZ in AW condition showing freshly formed martensite, Fe<sub>3</sub>C, cell boundaries, few undissolved MX type precipitates and high dislocation density; **b** selected area diffraction for Fe<sub>3</sub>C and MX precipitates

**Table 2** Transformation temperatures of INRAFM steel [9]

Sl. No	Transformation temperature with reference to Fe–C diagram	Kelvin, K	Centigrade, °C
1	Melting Temperature	1791 ± 5	1518 ± 5
2	Martensite Start, M <sub>s</sub>	640 ± 5	367 ± 5
3	Martensite Finish, M <sub>f</sub>	583 ± 5	310 ± 5
4	Recrystallisation Temperature (0.4 T <sub>m</sub> )	716 ± 5	443 ± 5
5	Austenite Start, Ac <sub>1</sub>	1091 ± 5	818 ± 5
6	Austenite Finish, Ac <sub>3</sub>	1130 ± 5	857 ± 5

dissolution, thereby leading to a matrix facilitating supersaturation of carbon. In fact, the fragmentation and dissolution of M<sub>23</sub>C<sub>6</sub> could also be credited for the development of precipitate-free grain boundaries in the SZ and in TMAZ.

The grain size distributions in the AW state in BM and SZ are shown in Fig. 6a and b. There is no obvious change in the grain size distribution in the AR material and unaffected BM region in AW state which is remote from the center of SZ. However, there has been substantial increase in the area fraction of very fine grains in SZ (Fig. 6b). These fine grains correspond to low-angle boundaries,

which can result from the reorganisation of plastic deformation induced dislocations in SZ into a low energy configuration comprising of cells and sub-grains. The dynamic recovery process that promotes these features occurs more quickly in the SZ matrix that is depleted with carbides.

At the employed rotational speed of 200 rpm, TMAZ in 12-mm plates appears to develop temperatures between Ac<sub>1</sub> and Ac<sub>3</sub>, whereas in case of 6-mm plates, the TMAZ and HAZ have seen temperatures less than Ac<sub>1</sub> [16]. In this study, in 12-mm-thick plates, the coarsening and coalescence of M<sub>23</sub>C<sub>6</sub> particles are noticed in the HAZ (Fig. 4b). Ripening of M<sub>23</sub>C<sub>6</sub> would result when the peak temperature experienced in HAZ is below Ac<sub>1</sub> (818 °C) but much above that of tempering temperature employed (760 °C) in AR state. In this investigation, no alpha-ferrite is found in HAZ at 200 rpm. However, transformation to alpha-ferrite has been reported earlier in 12-mm plates when the rotational speeds employed are 500 and 900 rpm [15]; at these higher rotational speeds, the HAZ has seen temperatures in the intercritical zone.

The drastic variation in microstructure in the AW condition across various zones is also reflected in the form of an inhomogeneous distribution of hardness (Fig. 7). The hardness in BM is around 200 HV. The SZ region is very hard due to the presence of martensite, very fine MC, high dislocation density and Fe<sub>3</sub>C. There is a drastic drop in hardness as the distance from SZ increases towards unaffected BM. A significant decrease in hardness is seen in HAZ with a value less than 200 HV. The low hardness in HAZ could be associated with the over tempering of microstructure which is portrayed in the form of coarsening and coagulation of M<sub>23</sub>C<sub>6</sub> particles (Fig. 4b).

The occurrence of carbide-free grain boundaries in SZ and TMAZ is undesirable; these boundaries can act as preferential sites for the promotion of grain boundary sliding and creation of intergranular cavities and cracks leading to intergranular fracture under creep conditions. It shall be recapitulated that RAFM steels are designed to have adequate creep resistance. Therefore, there is a necessity to restore the grain boundary M<sub>23</sub>C<sub>6</sub> in the SZ and TMAZ of FSW welds and homogenise the microstructure across the weld joint by designing appropriate post-weld heat treatments. These heat treatments should also be aimed at eliminating Fe<sub>3</sub>C in SZ and promoting the re-precipitation of M<sub>23</sub>C<sub>6</sub> on grain boundaries, and also cause the dissolution of coarse and coagulated M<sub>23</sub>C<sub>6</sub> precipitates in HAZ and re-precipitation of these at appropriate locations in the desired shape and size. Thus, PWHT is mandatory for AW material to obtain the microstructure and mechanical properties similar to those possessed in AR material, and it is crucial to minimize the

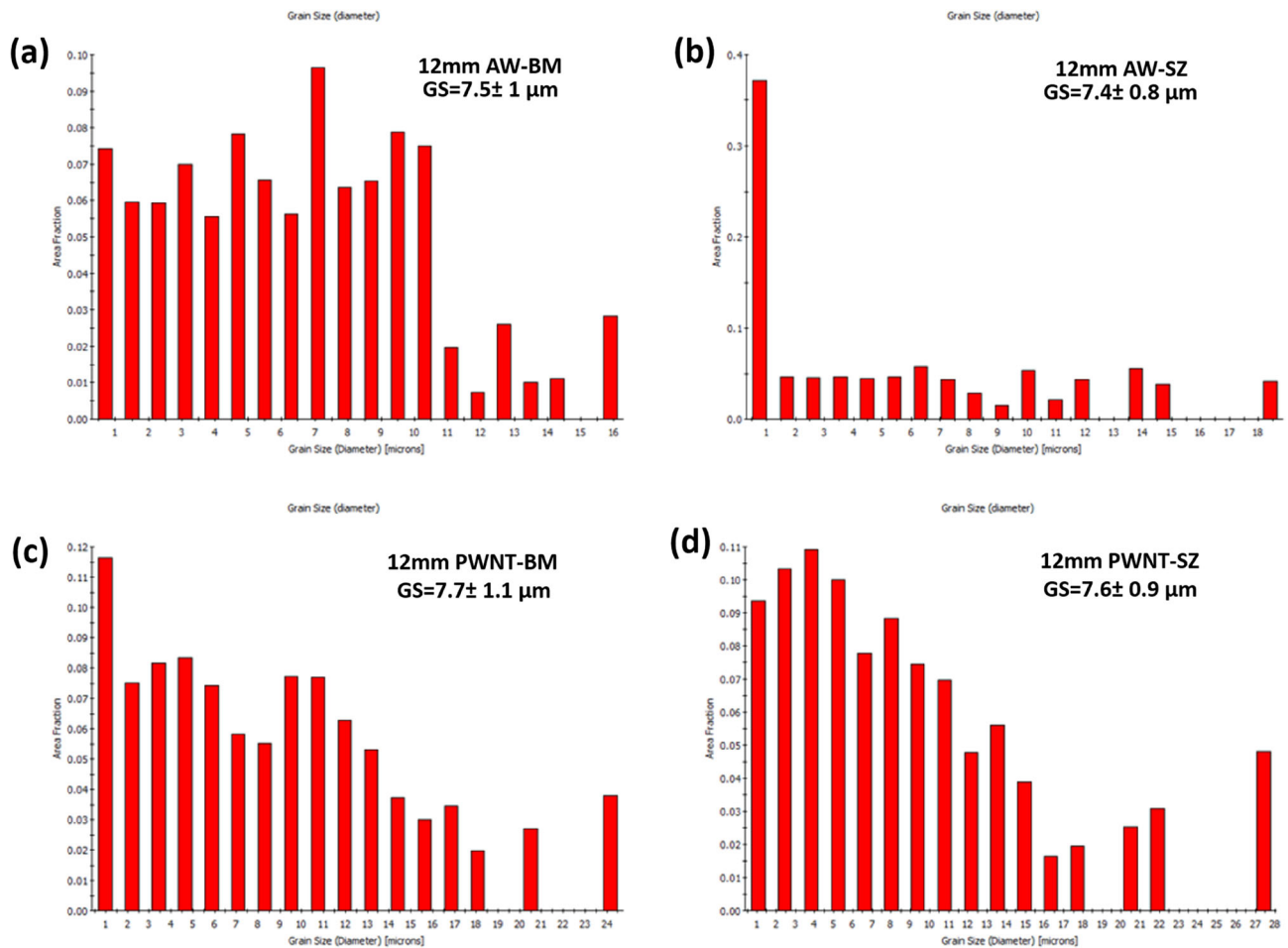


**Fig. 6** Grain size (GS) distribution obtained through EBSD **a** As-welded BM, **b** As-welded stir zone, **c** base metal after PWNT, and **d** stir zone after PWNT

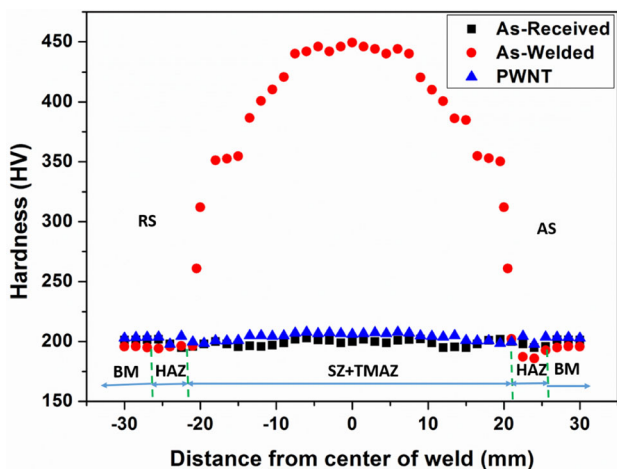


**Fig. 7** Hardness distribution across the transverse cross section in the as-received, as-welded and PWNT states

impact of mechanical property variation associated with FSW.

### (iii) Post-Weld Heat Treatment

A critical assessment of microstructure conducted on as-welded 6-mm-thick plates after PWHT's lead to a clear indication that the PWNT treatment is beneficial in providing uniform microstructure within the weld zones as compared to that obtained after post-weld direct tempering. In view of this, the AW 12-mm-thick plates were subjected to PWNT treatment comprising of soaking at 980 °C for 30 min, followed by air-cooling to room temperature and subsequently given a tempering treatment at 760 °C for 90 min and air cooling. The solutioning temperature (980 °C) was set much above the  $A_{c3}$  temperature (857 °C) in order to facilitate the complete re-austenization process and enabling the complete dissolution of the coarse and coagulated  $M_{23}C_6$  in HAZ, martensite and  $Fe_3C$  in SZ. Tempering temperature and duration were identical as those adopted in AR state for BM. PWNT re-precipitates  $M_{23}C_6$  on grain and martensite lath boundaries and proves to be instrumental in creating more homogeneous and uniform microstructure within SZ, TMAZ and HAZ zones

(Fig. 8). The microstructure in these zones become very similar to the AR base metal microstructure. As a consequence, a very uniform hardness distribution is achieved after PWNT and the hardness in the welded region is very much comparable to BM (Fig. 7). Grain size distribution of BM and SZ regions in PWNT state is incorporated in Fig. 6.

#### (IV) Tensile Properties of As-Received, Friction Stir Welded and Post-Weld Heat-Treated RAFM Steel

At a nominal strain rate of  $3.33 \times 10^{-4} \text{ s}^{-1}$ , the tensile properties of the alloy determined in AR, AW and PWHT states at various temperatures are given in Table 3. The monotonic tensile stress–strain curves evolved in AR, AW and PWNT states at different temperatures are shown in Fig. 9. The salient features pertaining to tensile properties, deformation and fracture are: (1) irrespective of the state prevailing, RAFM steel shows a decrease in 0.2% YS and UTS as the testing temperature increases, (2) strength of the alloy in AW state is higher at all the temperatures, (3) strength after PWNT treatment is very close or marginally higher than in AW state depending on the temperature, (4) ductility in the form of the percentage elongation exhibits a minimum at 450 °C in all the states, (5) ductility in AR state is better than in PWNT state at RT, 500 °C and 550 °C, (6) percentage elongation in PWNT condition is unusually higher compared to AW state at 450 °C, (7) tensile stress–strain flow curves in all the states exhibit a relatively short period of rapid strain hardening until UTS is reached, followed by very long period of softening at

elevated temperatures, and (8) in all the states at RT, the alloy exhibits monotonic strain hardening in the early stages followed by a regime of nearly stable peak stresses until the softening commences towards the end.

Based on the detailed investigations conducted on temperature dependence of tensile properties in the range 25–650 °C in the AR state, the loss of ductility at intermediate temperatures has been reported to result from the operation of dynamic strain ageing (DSA) process [17]. DSA is generally reported to occur due to the attractive interaction between diffusing solute species in the alloy and mobile dislocations during the deformation [18, 19]. Ageing of mobile dislocations by solute atmospheres would occur either during quasi viscous type of dislocation motion [20] or during the period when the dislocations are temporarily held up at local obstacles in the glide plane [21, 22]. The generally seen manifestation of DSA is the occurrence of serrations in the tensile flow curves and has been attributed to either locking or unlocking of mobile dislocations with the solute atoms. In this investigation, the alloy displays smooth stress–strain curves at all the temperatures without evidence for serrated flow. The non-existence of serrated flow has also been reported earlier in the tensile tests performed over a wide temperature range on this RAFM steel [17]. If DSA is the predominant process operating at a particular temperature, one would also expect an instantaneous negative strain rate sensitivity (SRS) of tensile flow stress; this negative SRS manifests itself through a decrease in flow stress with an increase in strain rate at a given temperature during the progression of

**Fig. 8** Microstructure in PWNT state **a** base metal showing tempered martensite structure, **b** heat-affected zone, **c–d** re-appearance of carbides at prior austenite grain boundaries and intragranular precipitates in TMAZ and SZ, respectively

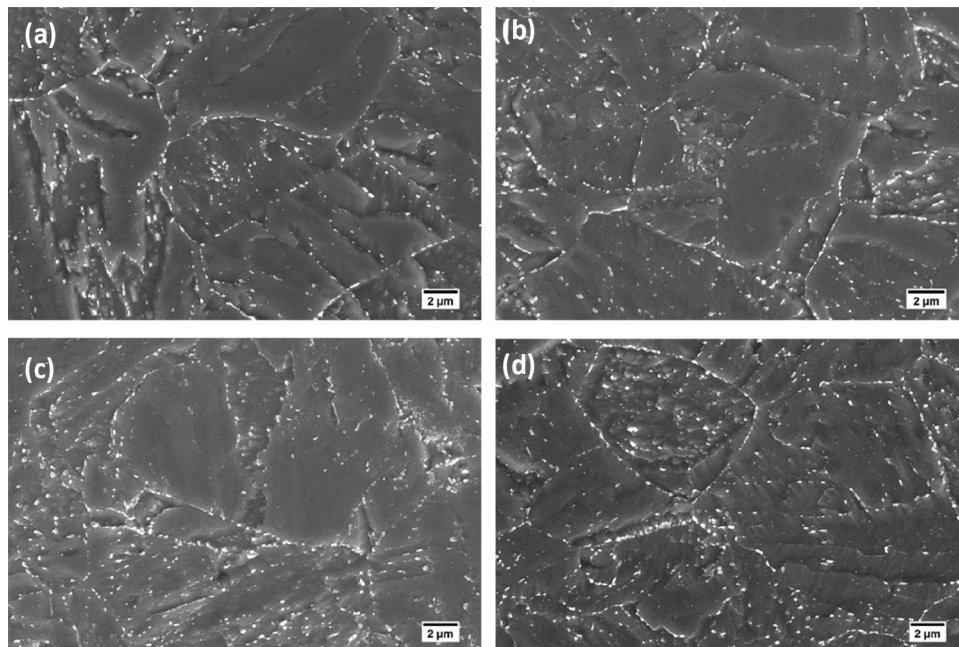




**Table 3** Results of the tensile tests performed on (a) as-received, (b) AW, (c) PWNT samples at RT and HT conditions

Sample condition	Test temperature (°C)	Yield strength (MPa)	UTS (MPa)	Elongation (%)
(a) AR	RT	476 ± 5.2	607 ± 8	23 ± 1.8
	450	397 ± 3.1	448 ± 4.2	12 ± 1.2
	500	367 ± 4.1	402 ± 5.8	29 ± 1.9
	550	329 ± 4.6	349 ± 5.1	33 ± 2.1
(b) AW	RT	513 ± 3.9	637 ± 4.9	15 ± 1.4
	450	473 ± 3.1	525 ± 4.2	12 ± 1.8
	500	418 ± 2.9	484 ± 5.1	14 ± 2.3
	550	368 ± 3.4	424 ± 4.3	15 ± 1.7
(c) PWNT	RT	473 ± 4.4	611 ± 5.9	21 ± 1.8
	450	410 ± 5.1	460 ± 6.1	18 ± 1.1
	500	376 ± 4.4	422 ± 5.1	20 ± 1.7
	550	348 ± 4.8	381 ± 6.4	21 ± 2.3

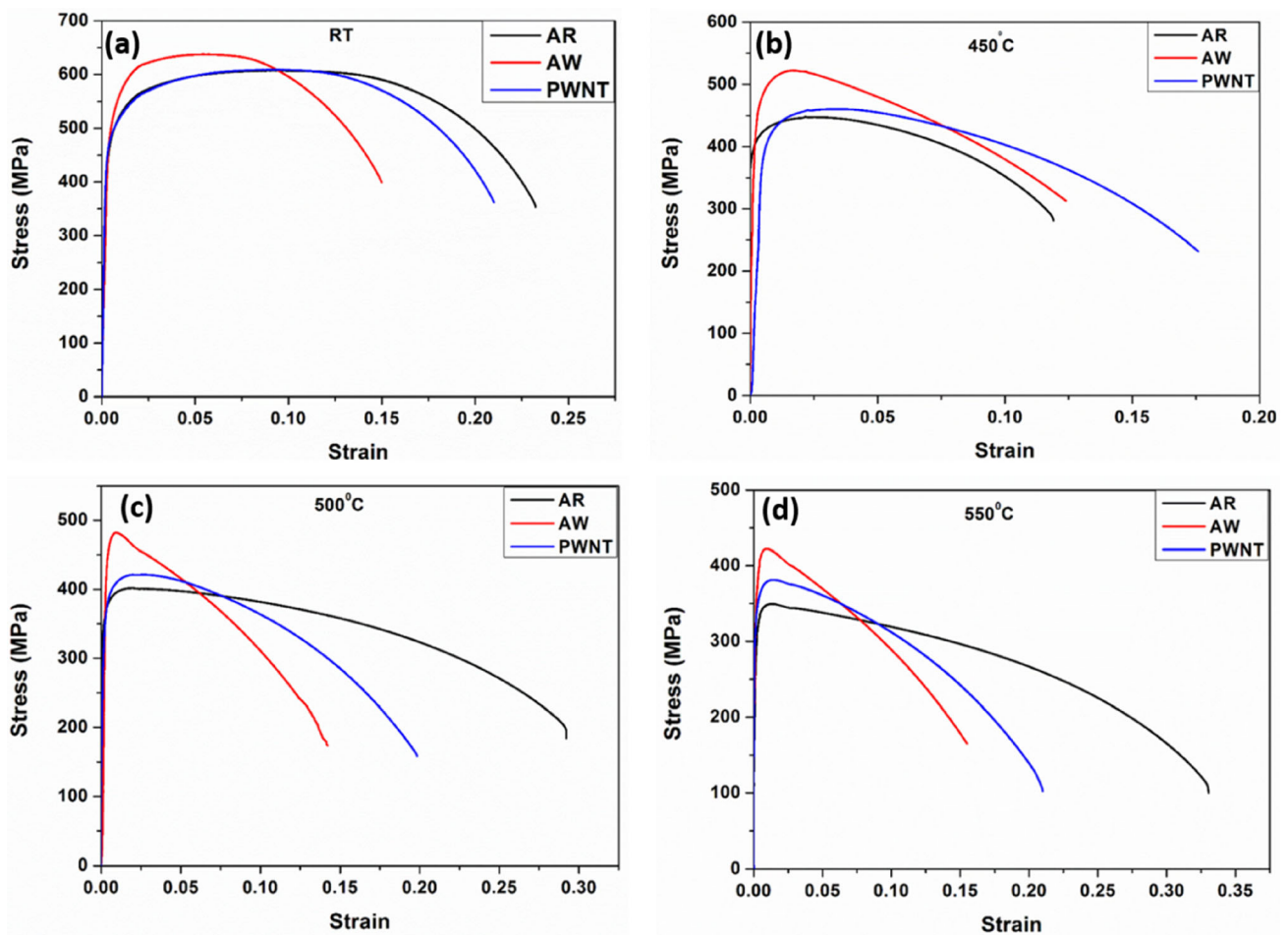


**Fig. 9** Tensile stress–strain flow curves of the AR, AW and PWNT conditions tested at **a** RT, **b** 450 °C, **c** 500 °C, **d** 550 °C

the tensile deformation. Vanaja et al. [17] examined the SRS at room temperature and 300 °C; these studies clearly indicate that the SRS remains positive at room temperature,

and negative at 300 °C where DSA prevails. In the domain where DSA is absent, the positive strain rate sensitivity results. Negative strain rate sensitivity is considered as a

potent indicator of DSA than the display of serrated flow [19]. The low ductility observed at 450 °C in this investigation could be credited to DSA.

In general, many of the solution annealed stainless steels and superalloys exhibit rapid strain hardening in DSA regime. On the other hand, the ferritic-martensitic steels exhibit strain softening predominantly at elevated temperatures as displayed in Fig. 9. This type of softening is akin to that reported earlier during low cycle fatigue of cold-worked 304 stainless steel [23], and modified 9Cr1Mo steel [24] from which RAFM steel has been derived. Softening of RAFM steels having high initial dislocation densities could result when the annihilation rate of dislocations is greater than the generation rate causing a net decrease in dislocation density, or when the rearrangement of dislocations takes place into a cell or sub-grain structure resulting in an increase in the mean free path for dislocations. Annihilation of lath boundaries can also occur due to interaction between martensite lath boundary dislocations and mobile dislocations generated during tensile deformation. Softening may also result from the coarsening of  $M_{23}C_6$  precipitates. However, the observed softening in all the states cannot be attributed to coarsening of precipitates since the tensile tests are conducted at much lower temperatures than those mentioned to be conducive for coarsening of  $M_{23}C_6$ .

The EBSD analysis of the boundary maps taken from different zones of AW and PWNT samples can be used judiciously to explain the variation in tensile properties. Figures 10 and 11, respectively, describe EBSD image quality figures in AW and PWNT states and depict the volume fraction of low-angle grain boundaries (defined by misorientation angle  $2 \text{ deg.} \leq \theta \leq 15 \text{ deg.}$ ) and high-angle grain boundaries (misorientation angle  $\theta \geq 15 \text{ deg.}$ ). In the AW state, the volume fraction of LAGBs is very low in SZ compared to the values recorded in BM, HAZ, and TMAZ. After PWNT treatment, LAGBs have increased in SZ and TMAZ. The increase in tensile elongation from the AW to PWNT condition can be attributed to the increase in the LAGB concentration owing to ease in dislocation movement. As the misorientation between adjacent grains is less, dislocation movement will be easier in regions having higher fraction of LAGBs and they contribute to increased ductility. The variation in the tensile behaviour of the AW and PWNT condition can be explained by this change in the fraction of LAGBs and HAGBs. LAGBs are considered as Read and Shockley dislocation arrays, and annihilation of such boundaries would occur by impingement of mobile dislocations [25]. At elevated temperatures, dislocation climb and cross-slip enhance the annihilation mechanism and promote the coarsening of laths, cells and sub-grains leading to much higher softening rates. At room temperature, the

reorganisation of dislocations into low energy configurations would be sluggish in the initial stages of deformation and therefore the flow stress response curves show an initial period of strain hardening as revealed in Fig. 9.

The hardening (+)/softening (–) rates in the tensile tests conducted at various temperatures in AR, AW and PWNT states are summarised in Table 4 and Fig. 12. The hardening/softening rates are defined as: [(true stress corresponding to 0.1 strain- true stress at 0.05 strain)/0.05]. The total contribution to total elongation results from the combined action of deformation induced modifications in substructure and localisation of deformation due to necking towards the end of tensile testing; the later gets depicted in the form of transgranular ductile fracture (Fig. 13). The hardening/softening ratio described here predominantly portrays the changes occurring during tensile deformation and eliminates the contribution from the fracture process. The softening observed in tensile tests in all the states at elevated temperatures could be attributed to the cumulative effects of dislocation annihilation, or coarsening of laths, cells, and sub-grains. The rapid softening in AW state that is described in Fig. 9 could also be considered to result partially from the annihilation of dislocations at HAGBs in SZ.

#### (E) Fracture Modes

Irrespective of the material state, fracture at all the temperatures is in ductile transgranular mode characterized by the presence of dimples (micro voids) on the fracture surface. Typical fracture surfaces of samples fail at 500 °C in the AR, AW and PWNT states and are illustrated in Fig. 13a, b and c, respectively. Fracture in all weld and PWNT samples occur at the interface between the HAZ and base metal. Figure 13 d represents the features on the fracture surface of AW sample tested at 450 °C, where the failure has been found in the vicinity of microstructurally altered BM (HAZ) region of low hardness. In spite of low ductility at 450 °C, no intergranular cavities or cracks are noticed in any of the states. The inset in Fig. 13d represents the low-magnification view of the fracture surface.

## 4 Conclusions

(i) The 12-mm-thick as-received RAFM steel displayed a tempered martensite microstructure. TEM studies revealed  $M_{23}C_6$  type carbides on prior austenite grain and martensite lath boundaries. The finer particles in the intra-lath regions were identified as Ta- and V-rich MX type of carbides and carbonitrides. (ii) Bead-on-plate FSW was successfully accomplished by employing PCBN tool with a rotational speed of 200 rpm. In the as-welded state, the weld joint was composed of SZ, TMAZ, HAZ and unaltered base

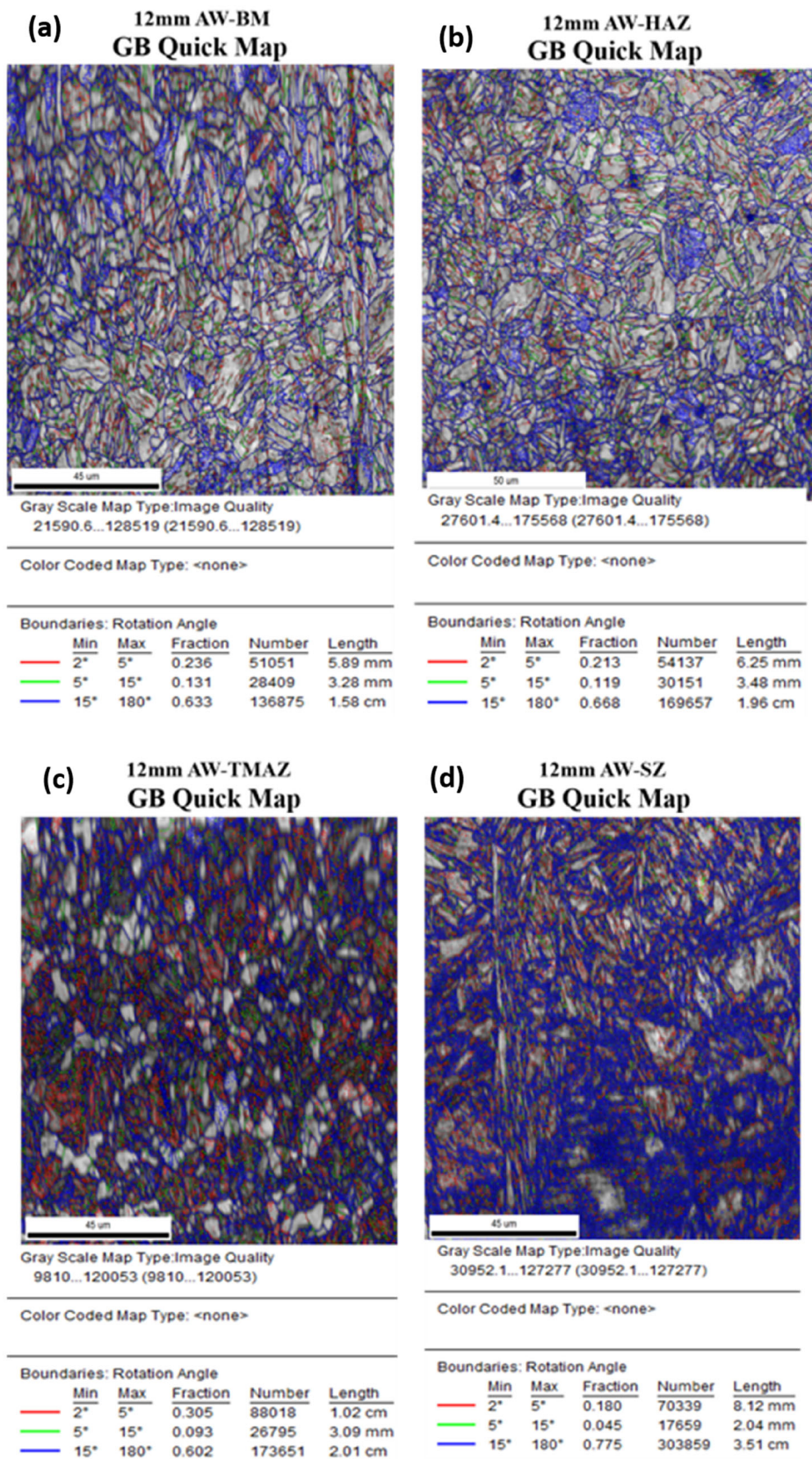


**Fig. 10** EBSD image quality maps obtained in as-welded state. These maps illustrate both low- and high-angle boundaries comprising of cell, sub-grain, lath and grain boundaries in **a** base metal, **b** HAZ, **c** TMAZ and **d** SZ. Incorporated table contains angle of boundaries, their fraction, number, and length



**Fig. 11** EBSD image quality maps obtained in PWNT state. These maps illustrate both low- and high-angle boundaries comprising of cell, sub-grain, lath and grain boundaries in **a** base metal, **b** HAZ, **c** TMAZ and **d** SZ. Incorporated table contains angle of boundaries, their fraction, number, and length

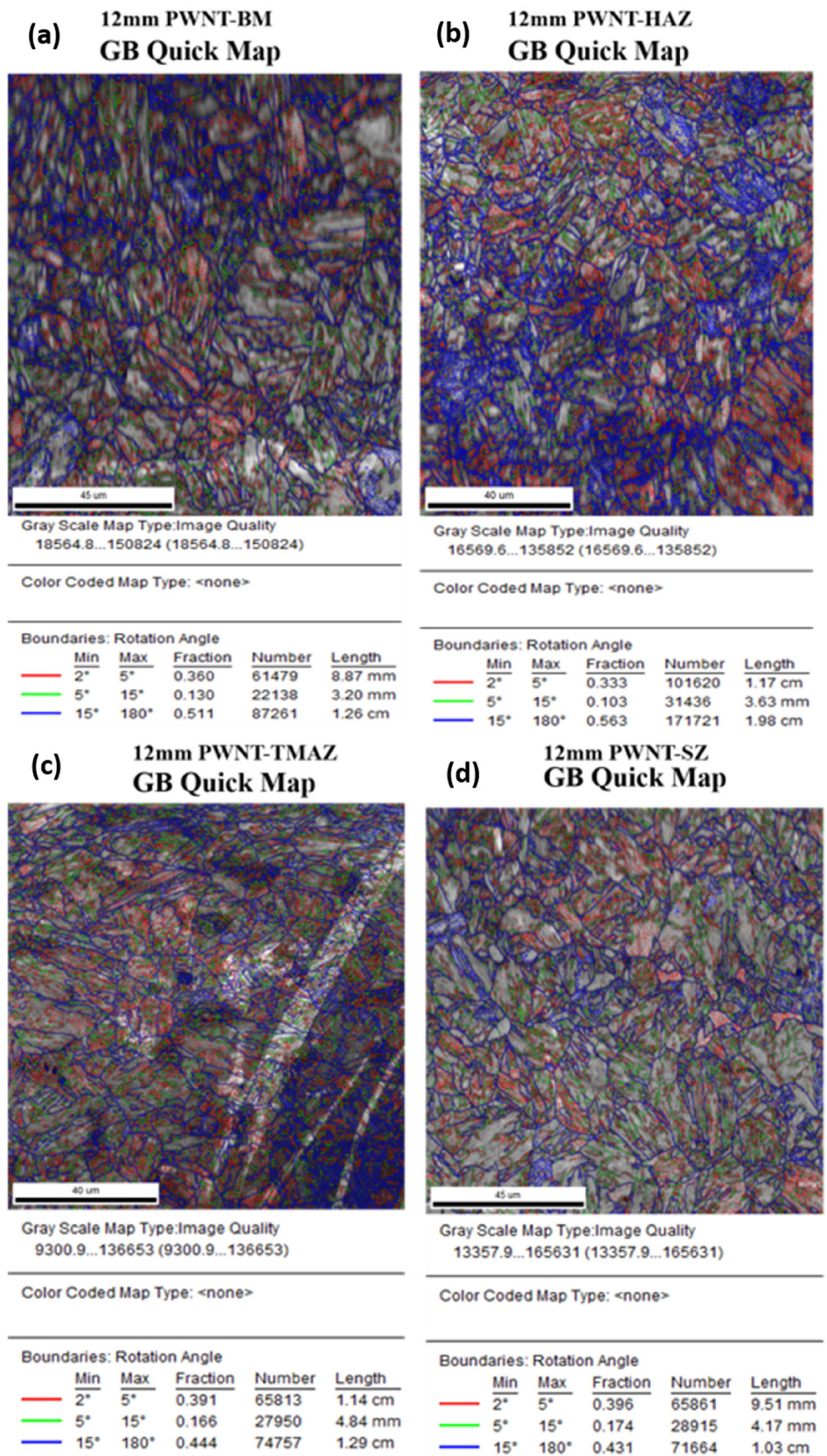


**Table 4** Hardening (+) softening (–) rates of different samples at different test conditions

Sample condition	Hardening (+)/softening(–) rates at test temperatures			
	RT	450 °C	500 °C	550 °C
AR	+ 817	– 1391	– 46	– 80
AW	+ 265	– 1720	– 1895	– 1412
PWNT	+ 839	– 711	– 644	– 717

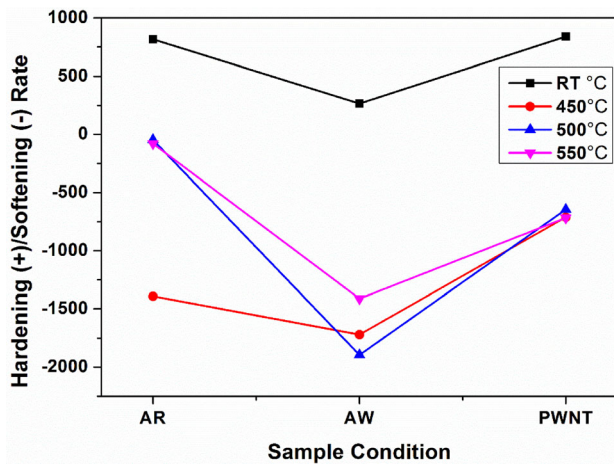
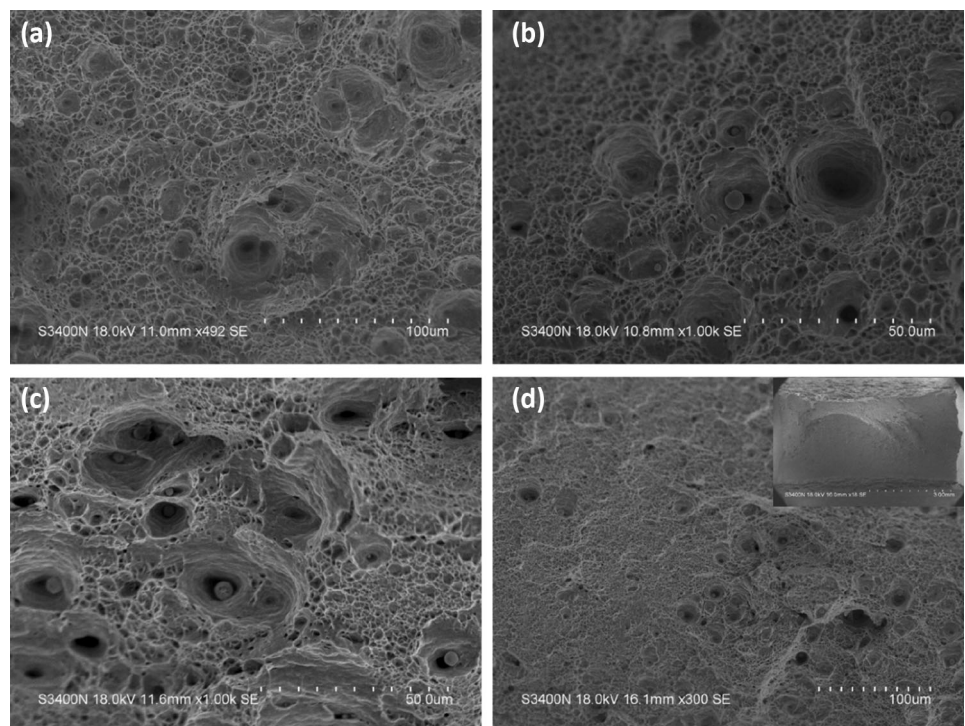


**Fig. 12** Hardening/softening rates for different states at different temperatures

metal. (iii) SZ displayed very high hardness due to the presence of martensite, Fe<sub>3</sub>C and high dislocation density. The SZ and TMAZ exhibited precipitate-free prior austenite grain boundaries which acted as preferential sites for the occurrence of grain boundary damage under creep conditions, while HAZ displayed ripening and agglomeration of carbides with concomitant decrease in hardness. (iv) The as-welded microstructure was completely modified and restored to the parent metal microstructure by PWNT treatment. The non-uniformity in hardness across the transverse section was also eliminated. (v) Tensile tests conducted in different states over the wide temperature range indicated UTS to be in the order AW > PWNT > AR, while ductility in the form of the percentage elongation is in the order AW < PWNT < AR. An exception to this generalisation was shown at 450 °C, where the

**Fig. 13** Fractographs of the samples tested at different conditions **a** AR-500 °C, **b** AW-500 °C, **c** PWNT- 500 °C, **d** AW-450 °C





ductility was in order  $AR < AW < PWNT$ . (vi) Irrespective of the state, the minimum in ductility was displayed at 450 °C owing to the prevalence of dynamic strain ageing. In all the states and at all the temperatures ductile fracture prevailed. (vii) Tensile flow stress–strain response revealed a brief period of monotonic hardening in all the states at room temperature, followed by softening. Elevated temperatures were found conducive for rapid softening. The variation in monotonic tensile stress response was rationalised on the basis of evolving substructure during tensile deformation. (viii) The tensile test samples were taken from the central portion of the bead-on-plate welds and represented the full penetration welds, as would also be expected from welding of two plates in a configuration of a butt joint. Thick sections may require FSW from both the sides when two plates joining is contemplated in butt configuration at very low rotational speeds; this is essential since tools of larger length would fail at low heat inputs associated with low rotational speeds.

**Acknowledgements** The authors acknowledge the financial support for this research from DAE-BRNS, Government of India. Some of the experimental facilities used to execute this work were supported by DST-FIST and DST-PURSE programs at the University of Hyderabad. The support received from Shri E. Rajendra Kumar and Shri Shiju Sam of IPR, Gandhinagar, is gratefully acknowledged.

## References

- Baluc N, Gelles D S, Jitsukawa S, Kimura A, Klueh R L, Odette GR, van der Schaaf, B and Yu J, *J Nucl Mater* **367–370** (2007) 33. <https://doi.org/10.1016/j.jnucmat.2007.03.036>.
- Tanigawa H, Shiba K, Möslang A, Stoller R E, Lindau R, Sokolov M A, Odette G R, Kurtz RJ and Jitsukawa S, *J Nucl Mater* **417** (2011) 9. <https://doi.org/10.1016/j.jnucmat.2011.05.023>.
- Yu J, Huang Q and Wan F, *J Nucl Mater* **367–370** (2007) 97. <https://doi.org/10.1016/j.jnucmat.2007.03.236>.
- Huang Q, Li C, Li Y, Chen M, Zhang M, Peng L, Zhu Z, Song Y and Gao S, *J Nucl Mater* **367–370** (2007) 142. <https://doi.org/10.1016/j.jnucmat.2007.03.153>.
- Van Der Schaaf B, Gelles D S, Jitsukawa S, Kimura A, Klueh R L, Möslang A and Odette G R, *J Nucl Mater* **283–287** (2000) 52. [https://doi.org/10.1016/S0022-3115\(00\)00220-8](https://doi.org/10.1016/S0022-3115(00)00220-8).
- Saroja S, Dasgupta A, Divakar R, Raju S, Mohandas E, Vijayalakshmi M, Bhanu Sankara Rao K, Raj B, *J Nucl Mater* **1** (2011) 53.
- Raj B and Jayakumar T, *J Nucl Mater* **417** (2011) 72. <https://doi.org/10.1016/j.jnucmat.2011.02.032>.
- Raj B, Rao K B S and Bhaduri A K, *Fus Eng Des* **85** (2010) 1460. <https://doi.org/10.1016/j.fusengdes.2010.04.008>.
- Raju S, Jeya Ganesh B, Rai A K, Mythili R, Saroja S, Mohandas E, Vijayalakshmi M, Rao K B S and Raj B, *J Nucl Mater* **389** (2009) 385. <https://doi.org/10.1016/j.jnucmat.2009.02.030>.
- Klueh R L, *Trans Indian Inst Met* **62** (2009) 81.
- Mishra R S and Ma Z Y, *Mater Sci Eng R Rep* **50** (2005) 1. <https://doi.org/10.1016/j.mser.2005.07.001>.
- Threadgill P L, Leonard A J, Shercliff H R and Withers P J, *Int Mater Rev* **54** (2009) 49. <https://doi.org/10.1179/174328009X411136>.
- Thomas D G W M, Nicholas E D, Needham J C, Murch M G, Temple-Smith P, Friction Stir Butt Welding, GB Pat. No. 9125978.8, Int. Pat. No. PCT/GB92/02203. **14** (1991) 3. <https://doi.org/10.1093/tropej/14.1.3>.
- Manugula V L, Rajulapati K V, Reddy G M, Mythili R and Bhanu Sankara Rao K, *Metall Mater Trans A Phys Metall Mater Sci* **48** (2017) 3702. <https://doi.org/10.1007/s11661-017-4143-5>.
- Manugula V L, Rajulapati K V, Reddy G M, Rajendra Kumar E and Rao K B S, *Sci Technol Weld Join* **23** (2018) 666. <https://doi.org/10.1080/13621718.2018.1467111>.
- Manugula V L, Rajulapati K V, Madhusudhan Reddy G, Mythili R and Bhanu Sankara Rao K, *Mater Des* **92** (2016) 200. <https://doi.org/10.1016/j.matdes.2015.12.019>.
- Vanaja J, Laha K, Sam S, Nandagopal M, Panneer Selvi S, Mathew M D, Jayakumar T and Rajendra Kumar E, *J Nucl Mater* **424** (2012) 116. <https://doi.org/10.1016/j.jnucmat.2012.02.020>.
- Bhanu Sankara Rao K, Castelli M G and Ellis J R, *Scr Metall Mater* **33** (1995) 1005.
- Bhanu Sankara Rao K, Castelli M G, Allen G P and Ellis J R, *Metall Mater Trans A* **28** (1997) 347. <https://doi.org/10.1007/s11661-997-0137-z>.
- Cottrell A H, *Philos Mag* **44**(1953) 829. <https://doi.org/10.1080/14786440808520347>.
- Van Den Beukel A and Kocks U F, *Acta Metall* **30** (1982) 1027. [https://doi.org/10.1016/0001-6160\(82\)90211-5](https://doi.org/10.1016/0001-6160(82)90211-5).
- den Beukel A, *Acta Metall* **28** (1980) 965.
- Rao K B S, Valsan M, Sandhya R, Mannan S L and Rodriguez P, *Metall Trans* **24** (1993) 913. <https://doi.org/10.1007/BF02656512>.
- Nagesha A, Kannan R, Sastry G V S, Sandhya R, Singh V, Bhanu Sankara Rao K and Mathew M D, *Mater Sci Eng A* **554** (2012) 95. <https://doi.org/10.1016/j.msea.2012.06.021>.
- Sauzay M, Brillet H, Monnet I, Mottot M, Barcelo F, Fournier B and Pineau A, *Mater Sci Eng A* **400–401** (2005) 241. <https://doi.org/10.1016/j.msea.2005.02.092>.

**Publisher's Note** Springer Nature remains neutral with regard to jurisdictional claims in published maps and institutional affiliations.